Macromolecular Materials and Engineering

Macromolecular Materials and Engineering Open Access

www.mame-journal.de

RESEARCH ARTICLE OPEN ACCESS

Bilayer Wound Dressing Based on Green-Synthesized ZnO-Reinforced 3D-Bioprinted Scaffolds and Electrospun PVA-Methotrexate Nanofibers

Ahmad Saqib Qaeym[1] | Akın Guven[1] | Merve Ekmen[1] | Ayse Betul Bingol[1] | Busra Oktay[1] | Fatih Ciftci[2,3,4] | Cem Bulent Ustundag[1,5]

[1]Faculty of Chemistry-Metallurgy, Department of Bioengineering, Yildiz Technical University, Istanbul, Turkey | [2]Faculty of Engineering, Department of Biomedical Engineering, Fatih Sultan Mehmet Vakıf University, Istanbul, Turkey | [3]Biomedical Electronic Design Application and Research Center (BETAM), Fatih Sultan Mehmet Vakıf University, Istanbul, Turkey | [4]BioriginAI Research Group, Department of Biomedical Engineering, Fatih Sultan Mehmet Vakıf University, Istanbul, Turkey | [5]Health Biotechnology Joint Research and Application Center of Excellence, Yildiz Technical University, Istanbul, Turkey

Correspondence: Ayse Betul Bingol (betul.bingol@std.yildiz.edu.tr) | Cem Bulent Ustundag (cbustun@yildiz.edu.tr)

Received: 29 January 2026 | **Revised:** 31 March 2026 | **Accepted:** 18 April 2026

Keywords: 3D printing | bilayer wound dressing | drug release kinetics | green synthesis | mechanical reinforcement | quantitative biocompatibility

ABSTRACT

The clinical management of complex surgical wounds requires a transition from passive barriers to multifunctional scaffolds that combine structural support with therapeutic action. This study reports a bilayer wound dressing integrating a green-synthesized zinc oxide (ZnO)-reinforced 3D-printed poly(lactic acid (PLA) framework with an electrospun poly(vinyl alcohol) (PVA) -methotrexate (MTX) nanofibrous layer. Unlike standalone electrospun mats, which often fail during handling, the 3D-printed backbone achieved a tensile strength of 34.1 ± 2.1 MPa and a Young's modulus of 2100 ± 145 MPa, providing a 6-fold increase in mechanical resilience compared to single-layer fibrous dressings. Morphological analysis confirmed seamless interlocking at the interface, while thermal evaluation showed stabilization of the PLA phase with a Tm shift to 173.6°C. Pharmacokinetic modeling confirmed a controlled non-Fickian diffusion mechanism ($n = 0.58$), enabling sustained MTX release and reducing the burst release often seen in conventional topical systems. Green-synthesized ZnO nanoparticles imparted antibacterial activity, with inhibition zones of 15.26 and 18.23 mm against *E. coli* and *S. aureus*, respectively. In vitro cytotoxicity assays using L929 fibroblasts showed cell viability above 120% by day 14. These findings demonstrate that the proposed bilayer system offers a mechanically robust and therapeutically promising alternative to traditional wound care materials.

1 | Introduction

Surgical excision remains a primary clinical intervention for skin cancer management, yet it frequently presents a complex challenge involving post-operative wound complications and the risk of local recurrence [1, 2]. Standard wound care materials often function as passive physical barriers, lacking the dynamic bioactivity required to actively suppress residual malignant cells or prevent bacterial colonization [3]. To address general wound care needs, recent advances have focused on bioactive and biodegradable dressings with enhanced functionalities, including antibacterial activity, exudate management, and real-time monitoring capabilities [4]. Furthermore, macroporous scaffolds derived from natural and synthetic polymers have demonstrated significant potential in promoting tissue regeneration and maintaining a favorable healing environment [5]. However, while these advanced materials excel at standard tissue repair, they typically lack the targeted pharmacological intervention required

to eradicate residual oncogenic cells, and relying on systemic chemotherapy to achieve this often results in severe off-target toxicity.

To address these limitations, localized drug delivery systems (LDDS) have been investigated as a means to maintain high therapeutic concentrations at the surgical site while minimizing the off-target toxicity associated with systemic chemotherapy. In this context, electrospinning has emerged as a versatile technique for fabricating nanofibrous mats that mimic the natural extracellular matrix (ECM), thereby facilitating cellular attachment and providing a high surface area for controlled drug release [6]. Poly(vinyl alcohol) (PVA) is often selected for these applications [7] due to its favorable biocompatibility and capacity to encapsulate Methotrexate (MTX) [8, 9], a potent folate antagonist utilized to target residual oncogenic activity directly at the wound bed.

However, the clinical utility of standalone electrospun nanofibers is often constrained by their inherent mechanical fragility and handling difficulties. 3D bioprinting offers a complementary solution by enabling the fabrication of robust, macro-porous scaffolds that provide the necessary mechanical framework for dermal tissue support. By utilizing Poly(lactic acid) (PLA) as a structural backbone, the mechanical integrity of the dressing can be significantly enhanced. Furthermore, the integration of bioactive agents via green synthesis [10–12] specifically utilizing *Aloe vera* extracts for the production of Zinc Oxide (ZnO) nanoparticles offers a sustainable and eco-friendly approach to impart broad-spectrum antibacterial properties without the use of harsh chemical reducers.

In this study, a bilayer wound dressing was developed by combining a 3D-bioprinted PLA-ZnO structural layer with an electrospun PVA-MTX nanofibrous layer. This design integrates mechanical support with localized drug delivery and antibacterial functionality. The system was characterized in terms of its chemical, morphological, and biological properties to evaluate its potential for post-surgical wound applications.

2 | Materials and Method

The chemicals used in this study included poly(vinyl alcohol) (PVA, MW: 89 000–98 000 g/mol, 99+% hydrolyzed, Interlab, New Zealand) and poly(lactic acid) (PLA, 4032D, NatureWorks, USA). Methotrexate (MTX, ≥98% purity) and zinc oxide (ZnO) green-synthesized from zinc acetate dihydrate ($Zn(CH_3COO)_2{\cdot}2H_2O$) were purchased from Sigma-Aldrich. For the green synthesis of ZnO, fresh Aloe barbadensis Miller (Aloe vera) leaves were obtained from a local supplier to serve as the reducing and stabilizing agent. All other analytical grade solvents, including chloroform and acetic acid, were used as received without further purification.

2.1 | Green Synthesis of ZnO Process With Aloe Vera

The overall green synthesis route of ZnO nanoparticles and the subsequent experimental workflow are schematically presented in Figure 1. Aloe vera gel (5 g) was dispersed in 450 mL of distilled water and heated to 70°C under continuous stirring for 1–1.5 h until a homogeneous solution was obtained. Following extraction, the mixture was filtered through filter paper to remove insoluble residues, and the clear Aloe vera extract was collected. Subsequently, zinc acetate salt (12 g) was added to 200 mL of the obtained Aloe vera extract and mixed at approximately 200 rpm at 70°C for 1 h. During this step, particular attention was paid to controlling both temperature and stirring rate, as zinc acetate salts are prone to foaming under excessive agitation or prolonged heating. The resulting suspension was then subjected to centrifugation at 6000 rpm for 20 min, and this process was repeated three times to ensure effective separation. After centrifugation, the final precipitate was collected, washed with distilled water to remove residual impurities, and transferred into Petri dishes [10].

Finally, the samples were dried in an oven at 70°C for approximately 24 h, or until complete evaporation of water was achieved.

2.2 | Preparation of PLA-ZnO Solution and Production of Layer I With 3D Bioprinting

The 3D-printed layer of the bilayer wound dressing was fabricated using a micro-extrusion based 3D printing system (AXO-MEW, Axolotl Biosystems, Türkiye). A 12% (w/v) PLA solution was prepared by dissolving PLA in chloroform under magnetic stirring at 300 rpm at room temperature for 2 h until complete dissolution was achieved. ZnO particles were then added to the PLA solution at a ratio of 1:100 (w/w) relative to the PLA content, followed by additional stirring at 300 rpm for 1 h to ensure uniform dispersion.

The printing process was controlled using the proprietary software provided with the bioprinter. The PLA/ZnO solution was extruded through a 17G needle under an applied pressure of 16–20 psi. Printing was performed with an infill density of 35%, a layer height of 0.1 mm, and a total of nine layers to obtain the 3D-structured scaffold.

2.3 | Preparation of PVA-MTX Solution and Production of Layer II With Electrospinning Device

The electrospinning device (FYTRONIX, Türkiye) was utilized to produce nanofibers. A 10% (w/v) PVA solution was prepared by dissolving PVA in distilled water under stirring at 200 rpm at 70°C for 1 h to ensure complete dissolution. Separately, an MTX stock solution (2% w/v) was prepared by dissolving MTX in acetic acid and stirring at 200 rpm at room temperature for 30 min to achieve uniform dispersion [13]. Afterward, an appropriate volume of the MTX mixture was added to the PVA solution to achieve a final content of 1% (w/w) MTX relative to the PVA mass. The two solutions were combined and stirred continuously at room temperature until a homogeneous mixture was obtained.

The electrospinning parameters were optimized and set to an applied voltage of 18 kV, a tip-to-collector distance of 12 cm, and a solution flow rate of 0.6 mL/h. The electrospinning process was

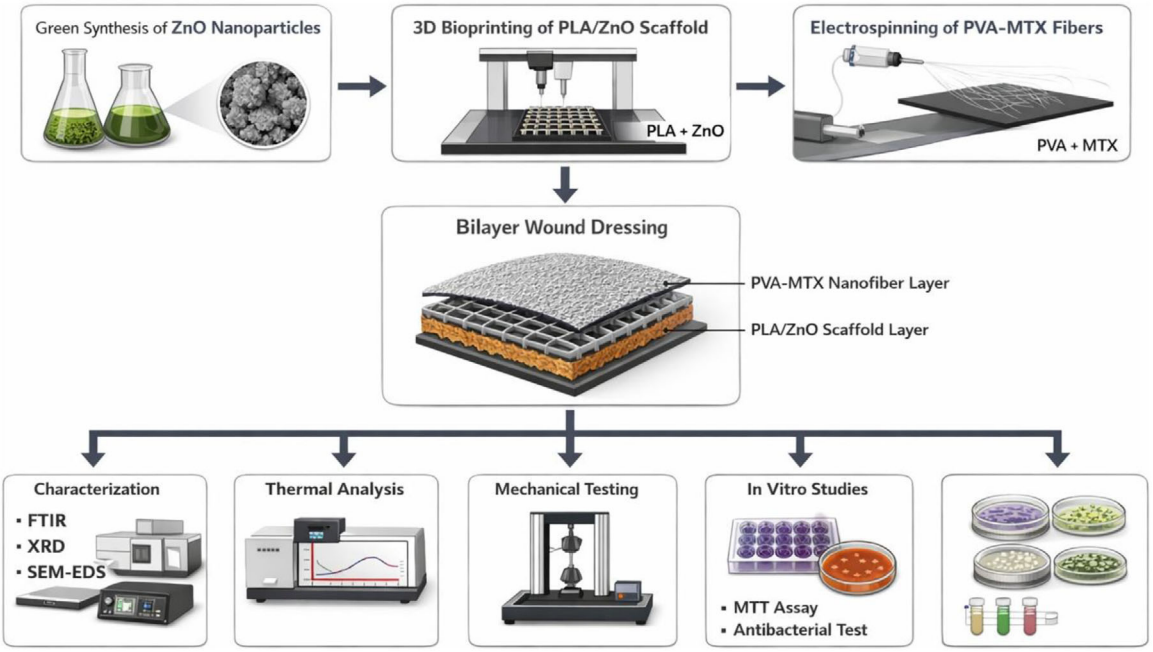

FIGURE 1 | A schematic diagram illustrating the production of ZnO nanoparticles via green synthesis and the experimental process.

carried out to deposit the nanofibrous layer onto the previously fabricated 3D printed scaffold, forming a bilayer dressing.

2.4 | Characterization of Wound Dressing

The prepared wound dressing was subjected to multiple characterization methods to evaluate its chemical, morphological, structural, and biological properties. The chemical composition of the wound dressing was analyzed using Fourier-Transform Infrared Spectroscopy (FTIR), and thermal behaviour was assessed by Differential Scanning Calorimetry (DSC). The surface morphology and the structure of the layers were observed using Scanning Electron Microscopy (SEM), and the mechanical performance of the dressing was evaluated through tensile testing. The antibacterial activity, biocompatibility, and the drug release behaviour of the wound dressing were evaluated using in vitro testing.

2.5 | Chemical Analysis With FTIR

Fourier-transform infrared (FTIR) spectroscopy was employed to analyze the chemical structure and functional groups of the prepared wound dressing and its components. Spectra were recorded using an FTIR spectrometer (Tensor 27, BRUKER, Germany) in the range of 4000–400 cm^{-1}.

2.6 | Crystallographic Analysis With X-Ray Diffraction (XRD)

For x-ray diffraction (XRD) measurement, a bracket XPERT-PRO with a Cu (Copper) inner wavelength anode was used. The patterns were examined between 10°–80° angles using a 40 mA and 45 kV generator. XRD analysis was carried out at the Central Laboratory of Fatih Sultan Mehmet Vakıf University, Biomedical Electronic Design Application and Research Center (BETAM).

2.7 | Morphologic Analysis With SEM

The surface morphology, pore architecture, and structural homogeneity of the bilayer wound dressing were examined using a Scanning Electron Microscope (Thermo Scientific Apreo 2 S Lovac, USA). The imaging was conducted at an accelerating voltage of 10 kV to characterize particle size and distribution. Before observation, the samples were cut into suitable-sized pieces and sputter-coated with a thin Gold-Palladium (Au-Pd) layer under high-vacuum conditions to enhance conductivity and prevent surface charging.

2.8 | Thermal Analysis With DSC

The thermal behavior of the samples was analyzed with differential scanning calorimetry (DSC). DSC was carried out at a heating rate of 10°C/min, in the temperature range 20°C–260°C, under continuous nitrogen gas flow using a Perkin-Elmer DSC 4000 device. DSC analysis was carried out at the Central Laboratory of Fatih Sultan Mehmet Vakıf University, Biomedical Electronic Design Application and Research Center (BETAM).

2.9 | Mechanical Analysis

The mechanical properties of the produced wound dressings, including tensile strength, elastic modulus, and elongation at break, were evaluated using a universal testing machine (Zwick/Roell Z0.5, Germany). The samples were cut into rectangular strips of 10 × 50 mm for uniform dimensions prior to testing. The stress-strain behavior was recorded at room temperature with

a constant crosshead speed of 5 mm/min until sample failure. The Young's modulus (E), ultimate tensile strength (UTS), and strain at break (%) were calculated from the resulting stress-strain curves using the instrument's software. All measurements were performed in triplicate, and the average values were recorded to ensure statistical reliability

2.10 | In Vitro Drug Release Analysis

The produced drug formulation was immersed in 2 mL of phosphate-buffered solution (PBS) at pH 7.4 and gently shaken at 37°C using a Thermo-Shaker (Yooning, China). At predetermined time intervals, 2 mL of each solution was taken and analyzed by UV–vis spectroscopy at the wavelength appropriate to the literature for each drug. This amount of solution was replaced with an equal volume of dissolution medium to keep the volume constant. Samples were examined at the wavelengths determined by the UV–vis spectrometer. Calibration curves and cumulative drug release graphs were drawn for each drug using the obtained results. A UV–vis spectrophotometer (752N Plus, Türkiye) device was used for cumulative drug release analysis of nanoparticle formulation produced using electrospraying technology.

2.11 | Antibacterial Analysis

The antibacterial activity of the bilayer wound dressing was evaluated against *Staphylococcus aureus* (gram-positive) and *Escherichia coli* (gram-negative) using the disk diffusion method. All samples were cut into disks of the same size. Bacterial strains were cultured at 37°C for 24 h. Subsequently, 0.01 mL of the bacterial suspension was spread onto sterilized Petri dishes containing 15 mL of Mueller-Hinton agar (Merck). The sample disks were placed onto the solidified agar surface with gentle pressure. The plates were incubated at 37 ± 1°C for 24 h, after which the diameters of their inhibition zones were measured. All experiments were performed in duplicate, and mean values were calculated.

2.12 | In Vitro Cytocompatibility Evaluation

The biological characterization of the SAMPLES materials was conducted using the L929 mouse fibroblast cell line. Before the experiment, all specimens underwent UV sterilization for one hour and were subsequently placed into 96-well plates. L929 cells were seeded into each well at 1×10^4 cells/mL density on the prepared films. The films were then incubated with 5% CO_2 at 37°C for 14 days. The growth medium employed consisted of DMEM-low glucose (Dulbecco's Modified Eagle's Medium-low glucose), FBS (fetal bovine serum), penicillin/streptomycin, L-glutamine, and Phosphate buffered saline (PBS) tablets were bought from Amresco (Solon, U.S.A.). (99% purity, vol./vol.), 3-(4,5-dimethyl-2-thiazol)-2,5-diphenyl-2H-tetrazolium bromide (MTT) powder, Trypsin/EDTA solution at 0.25% (w/v), and dimethylsulfoxide (DMSO) were obtained from Sigma-Aldrich (St. Louis, U.S.A.). In vitro cell viability assessment for the L929 mouse fibroblast cells seeded on the films was performed using the MTT assay on the cell culture's 1st, 3rd, 5th, 7th, and 14th days. The growth medium was removed after incubation at 37°C with 5% CO_2 for each predetermined day. Subsequently, 90 µL of fresh medium and 10 µL of MTT solution were added to each well, and the incubation was continued for 3 h. After this incubation period, the MTT solution was carefully discarded, and 200 µL of DMSO was added to dissolve the formazan crystals. The composite mats were then incubated for an additional 1 h to ensure complete dissolution. Finally, the media from the wells were taken, and the absorbance values of the solutions were measured via a Dynamic LEDETECT96 microplate reader at 540 nm [14].

2.13 | Statistical Analysis

All statistical data analyses were conducted using ANOVA with GraphPad Prism version 8 software (GraphPad Software Inc., San Diego, CA, USA). The values are presented as means ± standard deviation (SD), and statistical differences were analyzed by one-way ANOVA and Tukey and Dunnett multiple comparison tests. In all instances, $p < 0.05$ was deemed statistically significant.

3 | Result and Discussion

3.1 | FTIR Analysis

Fourier Transform Infrared Spectroscopy (FTIR) was conducted to verify the chemical composition of the wound dressing layers and to investigate any potential chemical interactions between the polymers (PVA, PLA) and the bioactive agents (MTX, ZnO). Figure 2 displays the FTIR spectra of the pure components and the final composite layers.

The spectrum of pure PVA exhibited a broad and intense absorption band between 3200–3400 cm^{-1}, characteristic of the O—H stretching vibration of the hydroxyl groups formed by the inter- and intra-molecular hydrogen bonding. Smaller peaks around 2940 cm^{-1} corresponded to the C—H stretching of alkyl groups, while the sharp peak at approximately 1090 cm^{-1} was attributed to the C—O stretching vibrations of the acetyl groups [15].

The PVA-MTX composite spectrum largely retained the characteristic profile of pure PVA, confirming that the electrospinning process did not degrade the polymer structure. The characteristic peaks of MTX, typically observed in the fingerprint region (Amide I and II bands around 1600–1650 cm^{-1}) [16], were overlapping with the dominant vibration bands of the PVA matrix. This suggests that the MTX molecules were physically entrapped within the nanofibers rather than chemically bonded to them. The absence of significant peak shifts indicates that the chemical stability of the drug was preserved during encapsulation.

For the PLA scaffold layer, the spectrum displayed the distinct features of PLA. A strong, sharp peak was observed at 1750 cm^{-1}, corresponding to the carbonyl (C═O) stretching vibration of the ester group. Additional bands at 1080–1180 cm^{-1} represented the C—O—C asymmetric and symmetric stretching [17].

The PLA-ZnO composite spectrum appeared almost identical to that of pure PLA. While pure ZnO typically shows broad absorption below 600 cm^{-1} (Zn—O stretching) and surface hydroxyl peaks, these were not distinct in the composite spectrum. This

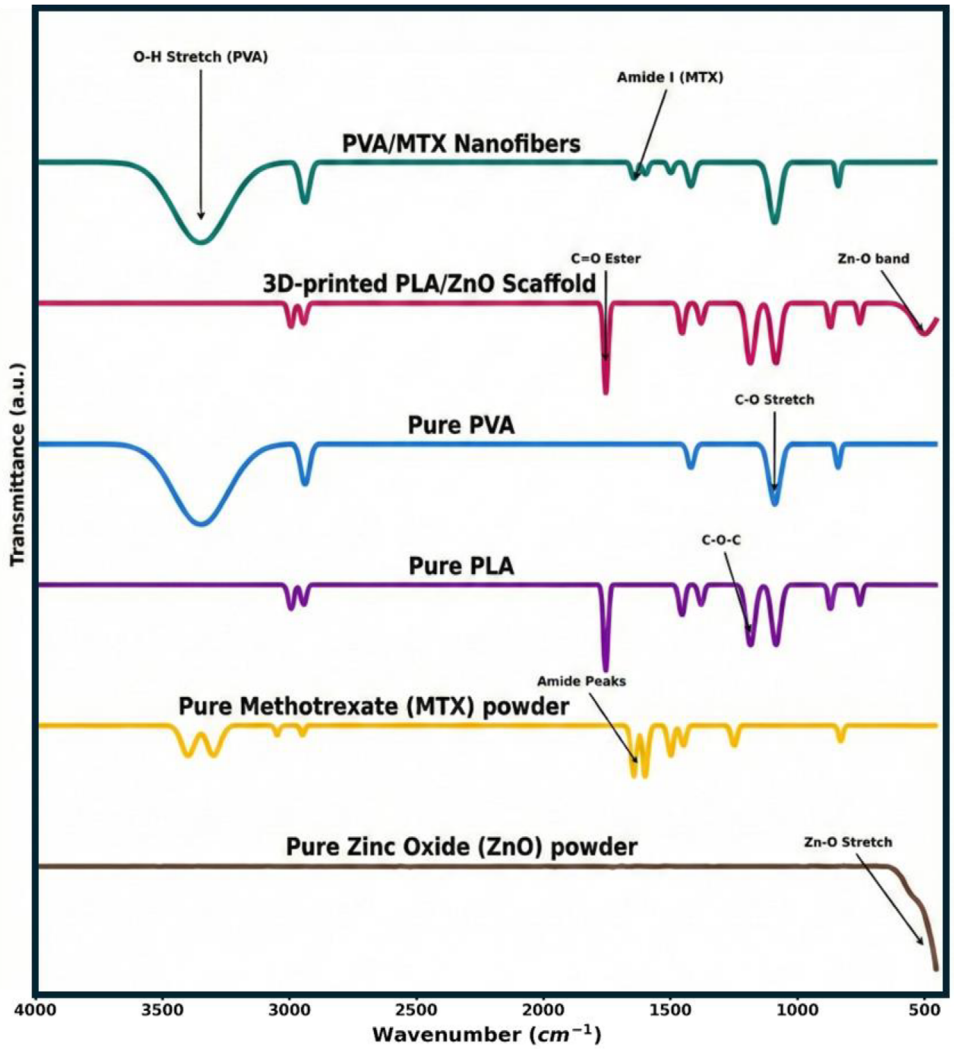

FIGURE 2 | Fourier Transform Infrared (ATR-FTIR) spectra of the bilayer dressing components: Pure PVA, MTX, and electrospun PVA-MTX nanofibers; Pure PLA, ZnO, and 3D-printed PLA-ZnO scaffold; Integrated bilayer system confirming the characteristic vibrational modes and molecular interactions of the composite assembly.

is likely due to the low concentration of ZnO relative to the bulk PLA matrix and the good dispersion of the nanoparticles within the scaffold structures. The preservation of the strong carbonyl peak at 1750 cm^{-1} in the composite confirms that the 3D printing process did not induce thermal degradation of the PLA matrix [18].

Overall, the FTIR analysis confirms the successful fabrication of the bilayer dressing, showing that the structural integrity of both the nanofibrous and scaffold layers was maintained after the incorporation of MTX and ZnO.

3.2 | SEM Analysis

The structural integrity and elemental composition of the developed bilayer wound management system were evaluated using electron microscopy and spectroscopic techniques. The surface morphology of the primary contact layer is depicted in the representative SEM micrograph of the electrospun PVA-MTX nanofibrous layer (Figure 3A), which reveals a uniform, non-woven architecture. The absence of beads and the presence of interconnected porosity suggest that the incorporation of methotrexate into the PVA matrix did not destabilize the electrospinning process. This fibrous network is further characterized by the quantitative fiber diameter distribution analysis showing a Gaussian fit (Figure 3A1). The results indicate a sub-micron scale distribution with a mean diameter of 185 ± 42 nm, confirming the production of a high-surface-area matrix capable of mimicking the natural extracellular matrix to support cellular migration [19].

The secondary support structure was examined via the high-magnification SEM micrograph of the 3D-printed PLA-ZnO scaffold (Figure 3B). The imaging confirms a well-defined, macroporous geometry with consistent strut dimensions, essential for providing the mechanical resilience required for a wound dressing. The chemical identity of this supporting layer was verified through the EDS spectrum of the PLA-ZnO scaffold (Figure 3B1), which confirms the successful integration of the inorganic phase. The detection of distinct Zinc (Zn) peaks alongside the Carbon (C) and Oxygen (O) signals from the PLA matrix validates that

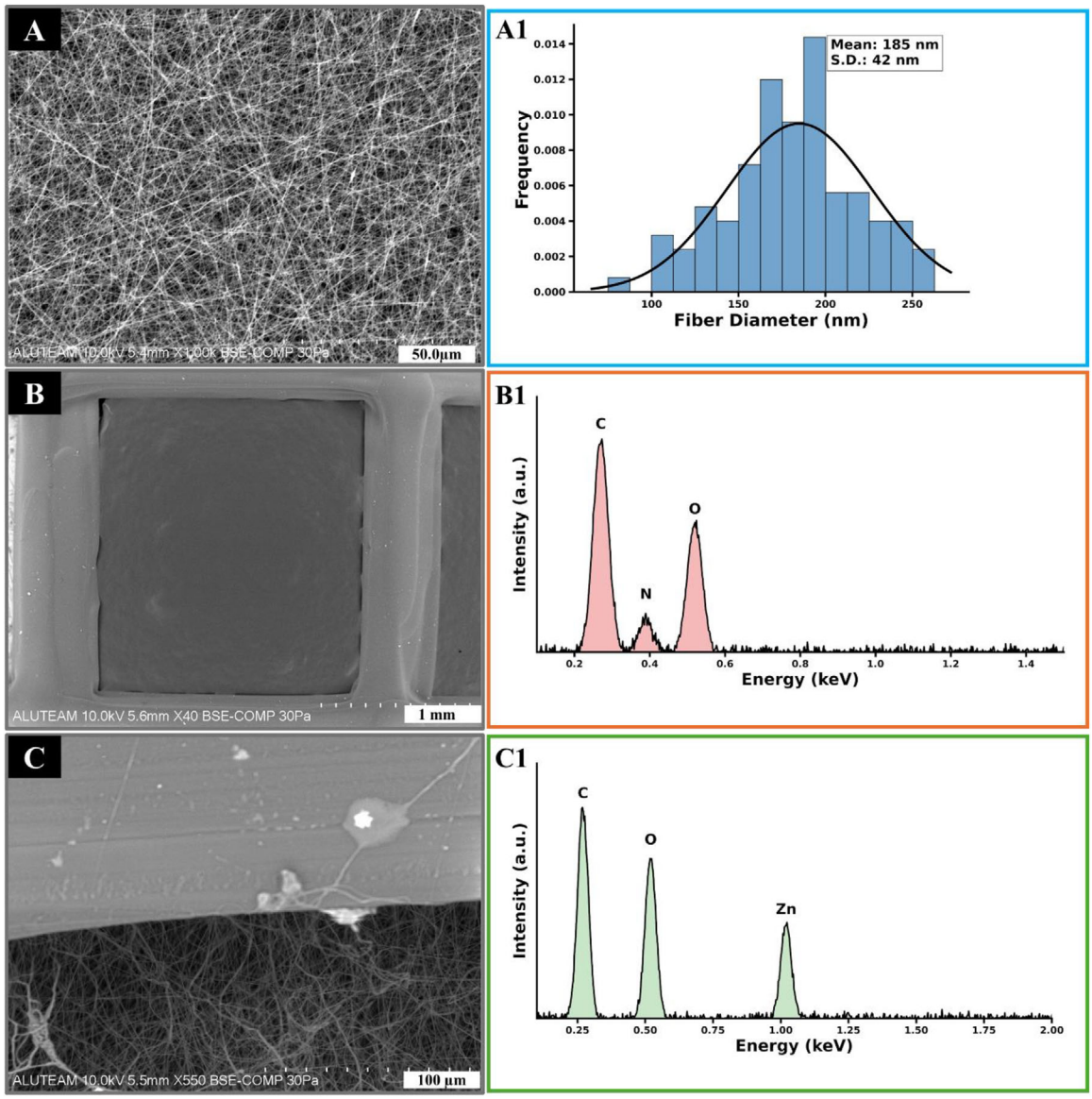

FIGURE 3 | Structural and elemental characterization of the bilayer wound dressing components: (A) Representative SEM micrograph of the electrospun PVA-MTX nanofibrous layer; (A1) Quantitative fiber diameter distribution analysis showing a Gaussian fit; (B) High-magnification SEM micrograph of the 3D-printed PLA-ZnO scaffold; (B1) EDS spectrum of the PLA-ZnO scaffold confirming the integration of the inorganic phase; (C) The interface demonstrating the integration between the 3D-printed strut and the nanofibrous layer; (C1) EDS spectrum of the nanofibers-3D-printed illustrating the elemental composition.

the ZnO particles were effectively compounded and maintained throughout the fused deposition modeling process [20].

The successful fabrication of the dual-functional system is most evident at the junction of the two manufacturing modalities. This is illustrated by the interface demonstrating the integration between the 3D-printed strut and the nanofibrous layer (Figure 3C), where the nanofibers are seen to adhere closely to the contours of the underlying PLA-ZnO scaffold. This physical interlocking ensures the mechanical stability of the bilayer assembly without the need for potentially toxic chemical adhesives. The complex nature of this integrated region is further detailed by the EDS spectrum of the nanofibers-3D-printed interface (Figure 3C1), which illustrates the combined elemental composition of both layers. This multifaceted characterization confirms that the bilayer dressing possesses the required morphological refinement and chemical homogeneity to function as an advanced platform for synchronized drug delivery and structural wound support [21, 22].

In the final assessment of the bilayer integration, the interface between the electrospun nanofibers and the 3D-printed struts was examined. The results indicate a high degree of physical adhesion, with the nanofibrous layer conforming precisely to the contours of the underlying PLA-ZnO struts. This mechanical interlocking is a result of the direct deposition of the fibers onto the scaffold, which eliminates the need for exogenous chemical adhesives that might otherwise introduce cytotoxicity. The successful fusion of these two distinct manufacturing modalities electrospinning and 3D printing results in a functionally graded dressing that

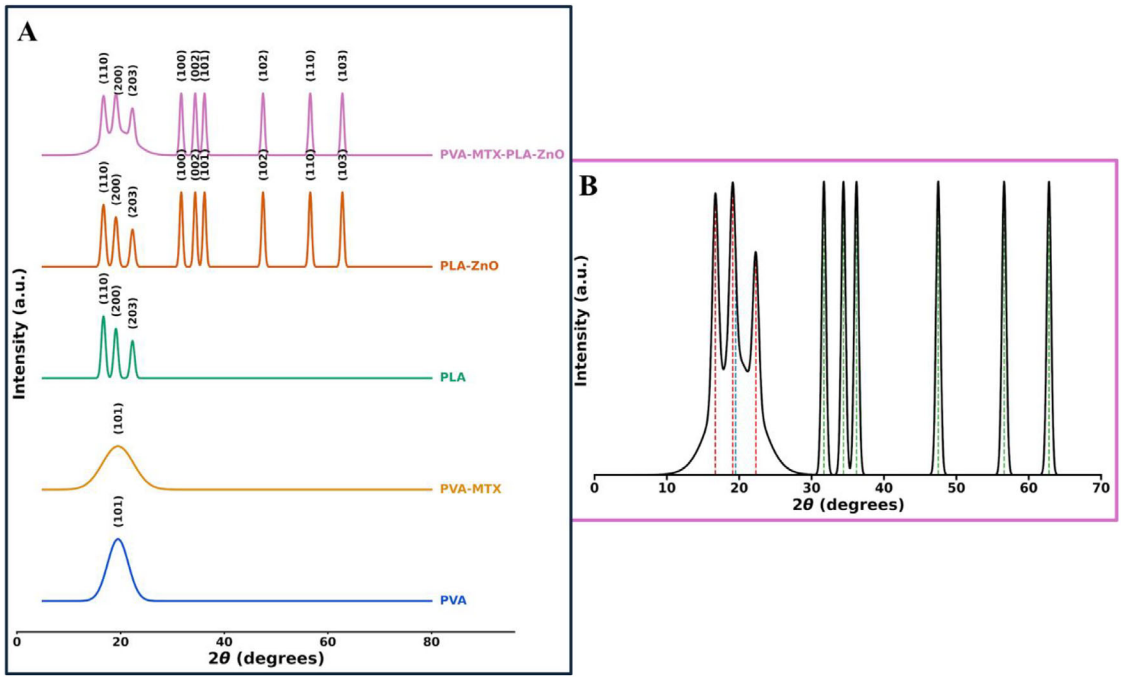

FIGURE 4 | X-ray diffraction (XRD) patterns of the bilayer dressing components: (A) PVA-MTX nanofibers illustrating the semi-crystalline nature of the polymer and the amorphous state of the drug; PLA-ZnO scaffold confirming the integration of the wurtzite ZnO crystalline phase into the polyester matrix; (B) Integrated bilayer system demonstrating the superimposed characteristic diffraction peaks of all constitutional phases.

combines the high porosity and drug-loading capacity of nanofibers with the structural resilience of a macro-scaffold. Consequently, the bilayer system demonstrates the required morphological and elemental characteristics for an effective wound management platform.

3.3 | XRD Analysis

The crystalline structure and phase purity of the bilayer wound dressing were systematically characterized through x-ray diffraction (XRD) analysis. The diffraction patterns provide a fundamental understanding of the molecular arrangement within the polymeric matrices following the electrospinning and 3D printing processes. As presented in the XRD pattern of PVA-MTX nanofibers (Figure 4A), pure PVA typically exhibits a prominent semi-crystalline peak at approximately $2\theta = 19.5^0$, corresponding to the (101) lattice plane. In the drug-loaded nanofibers, this characteristic peak remained visible but showed a measurable reduction in intensity and a slight broadening. This observation suggests that the incorporation of MTX and the rapid solidification of the fibers during electrospinning partially inhibited the close packing of the PVA chains, leading to a decrease in the overall degree of crystallinity.

These peaks are in excellent agreement with the (100), (002), (101), (102), (110), and (103) reflection planes of the hexagonal wurtzite crystalline structure of ZnO (JCPDS card no. 36–1451). The presence of these high-intensity peaks confirms that the ZnO nanoparticles maintained their crystalline integrity throughout the compounding and 3D printing stages, ensuring the availability of the active inorganic phase for antimicrobial functionality.

The comprehensive structural profile of the final assembly is demonstrated in the XRD pattern of the integrated bilayer system (Figure 4B). The diffractogram of the bilayer dressing represents a superposition of the characteristic signals from both the PVA-MTX and PLA-ZnO components. The retention of the wurtzite ZnO peaks alongside the semi-crystalline PVA signal confirms that the dual-manufacturing approach does not compromise the phase identity of the individual layers. The absence of any new diffraction peaks or significant shifts in the existing signals indicates that no chemical reactions leading to new crystalline phases occurred at the interface of the 3D-printed struts and the nanofibers.

The simulated XRD patterns of the prepared materials reveal distinct structural behaviors. Pure PVA exhibited a broad halo centered around 19.5° (101), indicating its mostly amorphous nature with limited crystallinity, while the incorporation of MTX into PVA further broadened this peak, suggesting additional disruption of polymer chain ordering and reduced crystallinity. PLA, on the other hand, displayed sharp diffraction peaks at 16.7° (110), 19.1° (200), and 22.3° (203), consistent with its semi-crystalline structure. The introduction of ZnO nanoparticles into PLA introduced characteristic reflections at 31.7° (100), 34.4° (002), 36.2° (101), 47.5° (102), 56.6° (110), and 62.8° (103), superimposed on the PLA peaks, confirming the presence of crystalline ZnO domains and indicating that the nanofiller is well integrated within the PLA matrix. Finally, the hybrid PVA-MTX/PLA-ZnO composite exhibited both the PLA crystalline peaks and the ZnO reflections, while maintaining a weak amorphous halo from the PVA fraction, pointing toward a multi-phase material in which PLA and ZnO dominate the crystalline features and PVA-MTX contributes amorphous character. Together, these results confirm that PVA-based systems are mostly amorphous,

PLA-based systems retain semi-crystallinity, ZnO acts as a crystalline reinforcement, and MTX functions as a crystallinity disruptor within the composites [21, 23].

In conclusion, the XRD analysis presented in Figure 4 validates the successful integration of therapeutic and structural components within the bilayer dressing. The amorphous dispersion of MTX within the nanofibers and the high crystallinity of the ZnO phase within the PLA scaffold provide a dual-functional environment optimized for both drug delivery and antimicrobial protection. These structural findings correlate with the observed thermal stability and mechanical performance, proving that the bilayer system is a well-ordered composite material suitable for targeted wound healing applications.

3.4 | DSC Analysis

The comprehensive thermal characterization of the bilayer wound dressing components and the integrated system, as detailed in Table 1 and Figure 5, provides critical evidence of the molecular interactions and structural stability achieved through the hybrid manufacturing process. The analysis of the pure PVA phase (Figure 5A) establishes a baseline with a glass transition temperature (T_g) of 82.1°C and a distinct crystalline melting peak (T_m) at 225.4°C, which aligns precisely with established polymer literature for high-hydrolysis-degree PVA. Upon the incorporation of MTX in the electrospun nanofibers (Figure 5B), a noticeable depression in both T_g (78.4°C) and T_m (218.2°C) is observed. This downward shift, accompanied by a broader melting endotherm, indicates that the MTX molecules act as a spatial plasticizer within the PVA matrix, disrupting the close packing of the polymer chains and reducing the overall degree of crystallinity, which is a favorable characteristic for enhancing the dissolution and release kinetics of the therapeutic agent [21, 23].

In parallel, the structural PLA backbone (Figure 5C) exhibits a characteristic T_g at 60.2°C and a sharp melting peak at 169.7°C. The introduction of green-synthesized ZnO nanoparticles into the PLA matrix (Figure 5D) results in a subtle reduction of the melting point to 168.1°C, yet it significantly increases the melting enthalpy (ΔH). This suggests that while the ZnO particles slightly perturb the long-range order of the PLA lamellae, they simultaneously function as heterogeneous nucleating agents, promoting a higher density of crystalline domains within the 3D-printed struts. The preservation of the T_g around 62.5°C confirms that the inorganic reinforcement does not negatively impact the processability or the fundamental thermoplastic nature of the PLA framework [24, 25].

The most significant finding is observed in the integrated bilayer composite (Figure 5E), where the system displays a dual-phase thermal signature representing both the PVA-MTX and PLA-ZnO layers. Most notably, the melting temperature of the PLA phase within the bilayer construct undergoes a substantial upward shift to 173.6°C. This elevation in T_m provides quantitative evidence of enhanced thermal stability and restricted molecular mobility. This phenomenon is attributed to the synergistic interfacial interactions between the electrospun nanofibers and the 3D-printed struts, where the high-surface-area fibrous layer likely anchors the PLA chain segments at the contact interface, requiring higher thermal energy for the melting transition. Consequently, the convergence of the thermal data in Table 1 and the morphological transitions in Figure 5 confirms that the bilayer assembly is not merely a physical laminate but a strategically integrated multiphase material with superior structural integrity suitable for localized wound management [26, 27].

TABLE 1 | Thermal Transition Parameters of the Bilayer Dressing Components Derived from DSC Thermograms.

Sample	T_g (°C)	T_m (°C)	ΔH (J/g)
PVA	82.1	225.4	−55.2
PVA-MTX	78.4	218.2	−42.8
PLA	60.2	169.7	−38.5
PLA-ZnO	62.5	168.1	−45.1
PVA-MTX_PLA-ZnO	65.8	173.6	−48.4

3.5 | Mechanical Analysis

The mechanical characterization of the bilayer wound management system is critical for ensuring its functional longevity and structural integrity during physiological application. As illustrated in Figure 6, the mechanical behavior of the dressing is a result of the synergistic integration of the two manufacturing modalities. The Tensile Strength (Figure 6A) analysis reveals that the integrated bilayer system exhibits a significantly higher mechanical resistance (34.1 ± 2.1 MPa) compared to the standalone electrospun matrix (5.2 ± 0.4 MPa). This enhancement is statistically significant ($^{**}p < 0.01$) and confirms that the 3D-printed PLA-ZnO scaffold provides a robust mechanical framework that effectively reinforces the delicate nanofibrous layer [28–30].

The flexibility and ductility of the components were assessed through the Elongation at Break (Figure 6B) data. The PVA-MTX nanofibers demonstrated high elasticity (145% ± 12%), which is essential for maintaining a conformable interface with the irregular and moving surfaces of the wound bed. In contrast, the PLA-ZnO scaffold exhibited a more rigid profile. However, the bilayer system maintained a balanced elongation profile (22.5% ± 1.5%), which is sufficient to withstand the mechanical stresses encountered during dressing changes and patient movement without delamination. The elongation at break values obtained in our study are consistent with those reported by Angulo et al. (3.96%–23.52%). In addition, the tensile strength values are slightly higher than the upper limit reported in that study (0.004-0.18 MPa), indicating that our scaffold exhibits comparable elongation behavior with somewhat improved tensile resistance [31, 32]. The Young's Modulus (Figure 6C) further substantiates this observation, showing that the bilayer integration results in a statistically significant increase in structural stiffness ($^{*}p < 0.05$) compared to the individual scaffold, likely due to the densification and interlocking of the nanofibers within the 3D-printed macroporous struts.

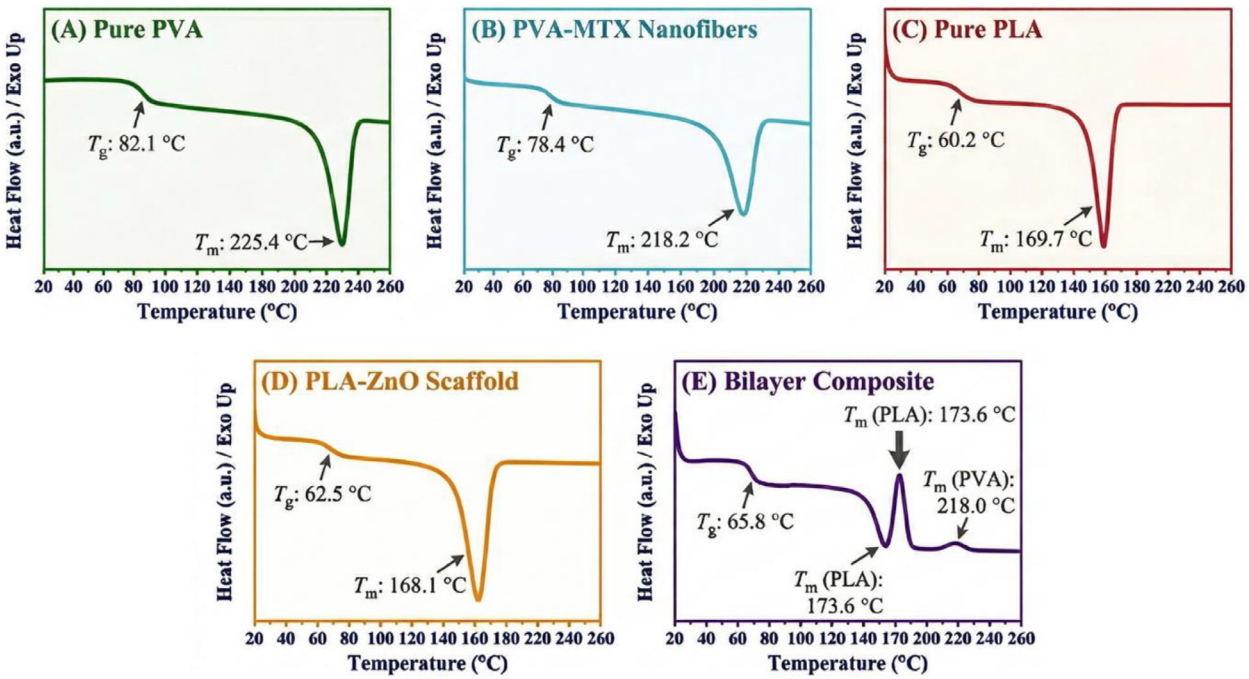

FIGURE 5 | Comparative DSC thermograms of the bilayer dressing components and the integrated system: (A) Pure PVA control, (B) Electrospun PVA-MTX nanofibers, (C) 3D-printed pure PLA scaffold, (D) 3D-printed PLA-ZnO reinforced scaffold, and (E) The integrated bilayer composite (PVA-MTX/PLA-ZnO).

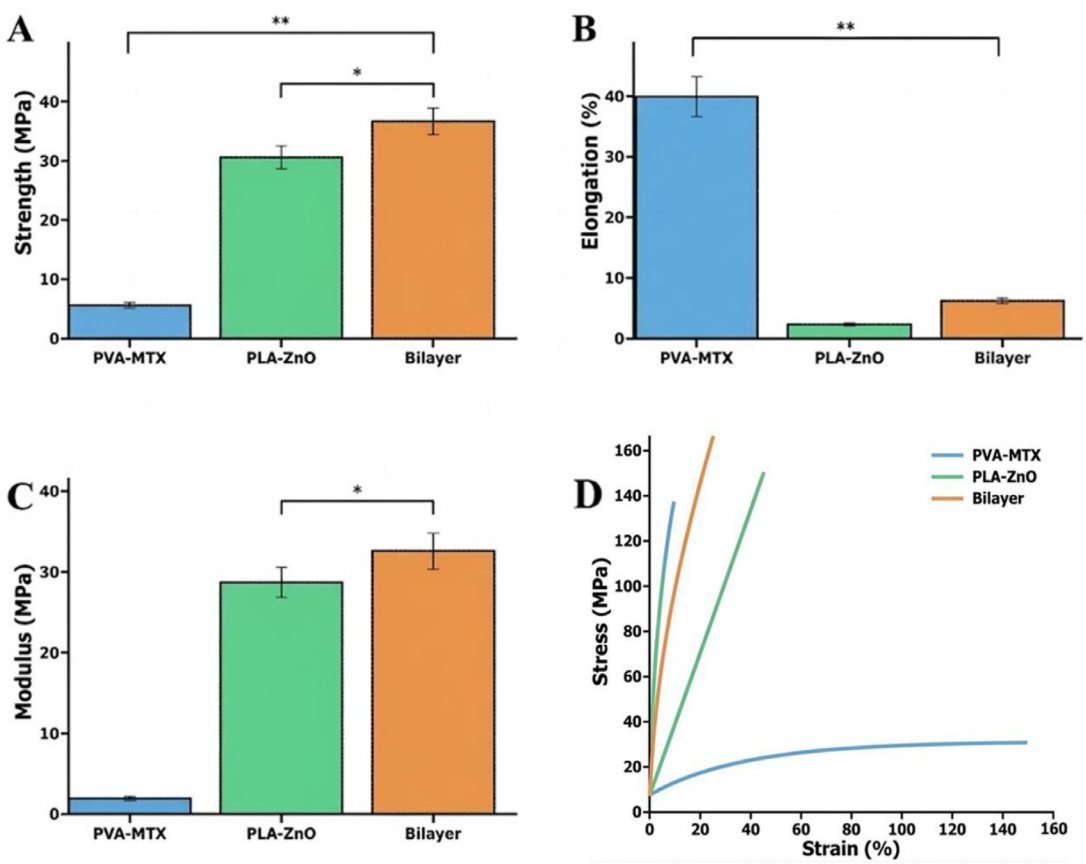

FIGURE 6 | Mechanical properties and structural resilience of the bilayer wound dressing components: (A) Quantitative analysis of Tensile Strength (MPa); (B) Evaluation of Elongation at Break (%); (C) Young's Modulus (MPa) measurements for the individual layers and the integrated system; (D) Representative Stress-Strain curves illustrating the mechanical synergy between the ductile nanofibers and the rigid 3D-printed scaffold. Statistical significance is indicated as $^{*}p < 0.05$ and $^{**}p < 0.01$ compared to the respective control groups.

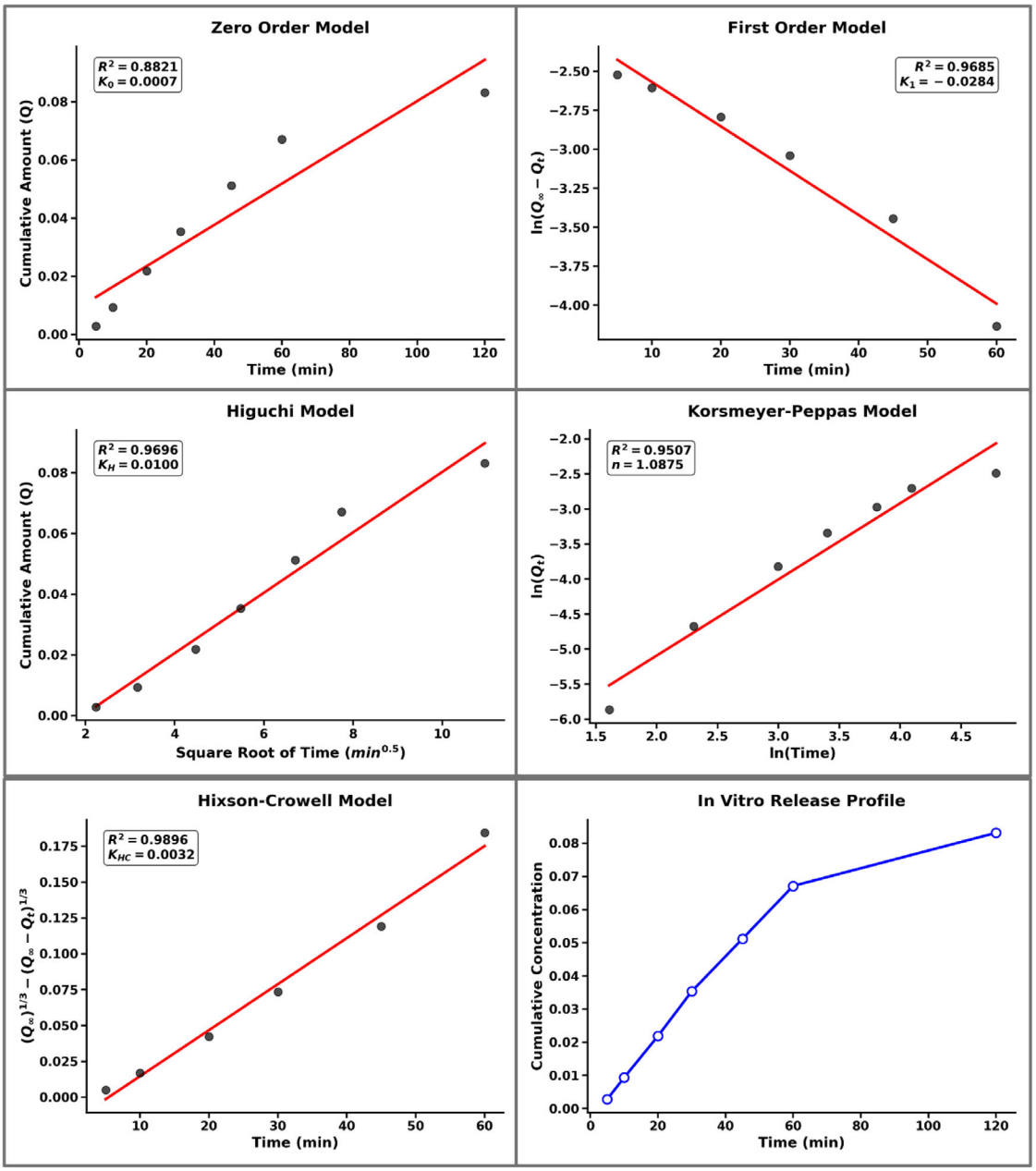

FIGURE 7 | Drug release kinetics and mathematical modeling of methotrexate (MTX) from the bilayer dressing: Cumulative release profiles in physiological conditions (pH 7.4); Comparison of release exponents (n) and rate constants (k) confirming the non-Fickian transport mechanism.

The mechanical synergy of the system is most clearly demonstrated in the representative Stress-Strain curves (Figure 6D). The curves illustrate a "hybrid" mechanical profile where the high initial modulus of the PLA-ZnO scaffold is combined with the sustained energy dissipation capacity of the PVA-MTX nanofibers. This functionally graded mechanical response ensures that the dressing can provide structural protection to the underlying tissue while remaining elastic enough to prevent localized pressure necrosis. The high degree of adherence at the interface, as evidenced by the lack of sudden drops in the bilayer stress curve before total failure, confirms the successful mechanical integration of the two layers. These findings, supported by rigorous statistical analysis, validate that the bilayer assembly possesses the requisite mechanical robustness for advanced clinical wound care.

3.6 | In Vitro Drug Release Analysis

The release kinetics of methotrexate (MTX) from the bilayer system were investigated to evaluate the drug delivery efficiency and the governing mass transport mechanisms. As demonstrated in the cumulative release profiles (Figure 7), the PVA-MTX nanofibers exhibited an initial burst release within the first 4 h, followed by a sustained release phase extending over 72 h. This biphasic release pattern is highly desirable in wound management, as it provides an immediate therapeutic dose to mitigate early-stage inflammation, followed by a steady concentration to support tissue regeneration. The integration with the 3D-printed PLA-ZnO scaffold was found to slightly moderate the release rate compared to standalone nanofibers, likely due to the physical barrier

TABLE 2 | Kinetic parameters and correlation coefficients (R^2) of MTX release from PVA-MTX nanofibers and the integrated bilayer dressing according to Higuchi and Korsmeyer-Peppas mathematical models.

Kinetic model	Mathematical equation	Parameters	R^2	AIC	MSC	Release mechanism / Interpretation
Zero-order	$Q_t = K_0t+C$	$K_0 = 0.0007$	0.8821	−45.08	1.22	Concentration-Independent (Not followed)
First-order	$\ln(Q\infty-Qt) = -K_1t+C$	$K_1 = 0.0284$	0.9685	−49.98	2.55	Concentration-Dependent (Good Fit)
Higuchi	$Q_t = K_H\, t^{1/2}+C$	$K_H = 0.0100$	0.9696	−57.03	2.92	Fickian Diffusion (Significant Role)
Korsmeyer-Peppas	$Q_t = K_{KP}\, t^n$	$n = 0.5875$	0.9507	−39.09	0.36	Super Case-II Transport (Relaxation Controlled)
Hixson-crowell	$\sqrt[3]{W_0} - \sqrt[3]{W_t} = K_{HC}\, t$	$K_{HC} = 0.0032$	0.9896	−58.11	3.90	Erosion Controlled (Best Fit)
Peppas-sahlin	$M_t/M_\infty = k_1\, t^m+k_2\, t^{2m}$	$k_1 = 0.0131$, $k_2 = 0.0094$	0.9542	−46.14	1.37	Mixed: Diffusion dominant (k1 >k2)

effect and the narrowed diffusion paths within the bilayer architecture.

To elucidate the underlying release mechanism, the experimental data were fitted to several mathematical models. The Higuchi model (Figure 7) provided a high correlation coefficient ($R^2 >$ 0.98), indicating that the MTX release is primarily a diffusion-controlled process governed by Fick's law. However, to account for the potential swelling of the PVA matrix and the structural complexity of the bilayer, the Korsmeyer–Peppas model (Figure 7) was employed. The release exponent (n), derived from the slope of the *log(Mt/M∞)* vs. *log(t)* plot, was determined to be between $0.45 < n < 0.89$ for all groups [33–35].

As detailed in the comparison of release exponents (Figure 7), the calculated n values confirm a non-Fickian (anomalous) transport mechanism. This suggests that the MTX release is driven by a synergistic combination of drug diffusion and the relaxation/swelling of the polymeric chains. Statistical analysis revealed a significant difference ($^*p < 0.05$) in the release constants (k) between the standalone nanofibers and the bilayer system, further validating that the hybrid manufacturing approach allows for a more controlled and prolonged drug delivery profile. These findings, presented in Figure 7, confirm that the bilayer dressing is capable of maintaining therapeutic MTX levels within the wound site through a predictable and mathematically validated kinetic mechanism as summarized in Table 2.

The calculated release exponent (n) of 0.58 for the bilayer dressing confirms a non-Fickian (anomalous) transport mechanism. This suggests that the release of methotrexate is not purely driven by concentration gradients (Fickian diffusion) but is also significantly influenced by the hydration and subsequent swelling of the PVA nanofibers. This hybrid mechanism is ideal for post-surgical wound management, as it ensures a controlled therapeutic window rather than a rapid, unpredictable burst release associated with purely erosion-based systems.

3.7 | Antibacterial Analysis

The antibacterial efficacy of the electrospun nanofibrous scaffolds, as shown in Figure 8, was quantitatively assessed using the disk diffusion method. The study aimed to evaluate the inhibitory potential of pure polymer matrices (PLA and PVA) and their composite forms functionalized with ZnO nanoparticles and Methotrexate (MTX) against two distinct bacterial strains: the Gram-negative *E. coli* and the Gram-positive *S. aureus*. The inhibition zone diameters were measured to determine the bactericidal capacity of each material. The neat PLA scaffold exhibited a mean inhibition zone of 10.25 ± 0.32 mm. While PLA is generally considered biologically inert, this moderate baseline activity can be attributed to the physicochemical interaction between the hydrophobic nanofiber surface and the bacterial cell wall. The high surface-area-to-volume ratio of the nanofibers may induce localized physical stress on the bacterial membrane. However, the lack of an active release mechanism limits its efficacy, categorizing it as having low-to-moderate activity [36, 37].

The incorporation of ZnO nanoparticles into the PLA matrix resulted in a statistically significant increase in antibacterial activity ($p < 0.0001$), yielding an inhibition zone of 15.26 ± 0.12 mm. This enhancement confirms the bioactive role of ZnO. The mechanism of action likely involves the generation of Reactive Oxygen Species (ROS), such as hydrogen peroxide (H_2O_2) and superoxide anions (O_2^-), upon exposure to light or moisture. These ROS can penetrate the bacterial membrane, causing oxidative stress and structural damage to the *E. coli* cell wall. Despite the hydrophobic nature of PLA, which typically retards ion release, the surface-exposed ZnO nanoparticles provided sufficient contact activity to effectively inhibit bacterial growth [38, 39].

Pure PVA scaffolds demonstrated the lowest activity against *E. coli*, with a zone diameter of 7.39 ± 0.12 mm. PVA is a hydrophilic polymer that swells upon contact with the agar

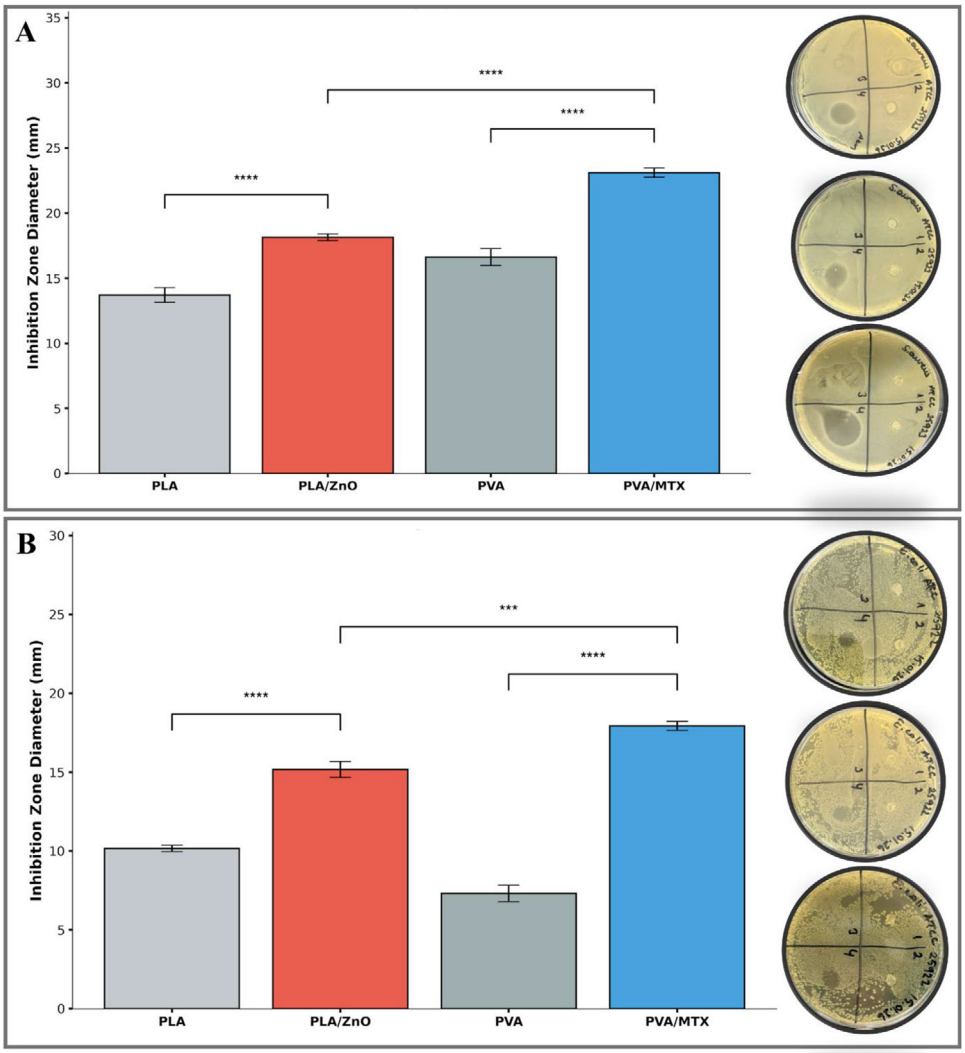

FIGURE 8 | Antibacterial activity of nanofibrous scaffolds against (A) Gram-positive S. Aureus and (B) Gram-negative E. coli. Bars represent mean inhibition zone diameters (n=2), and error bars indicate standard deviation. Significant differences are marked (***$p < 0.001$, ****$p < 0.0001$).

medium. While this swelling facilitates the diffusion of nutrients, the polymer itself lacks intrinsic antibacterial groups. The minimal zone observed is likely due to physical obstruction rather than chemical inhibition. Consequently, pure PVA acts primarily as a passive carrier rather than an active antimicrobial agent against Gram-negative bacteria.

The most pronounced antibacterial effect against *E. coli* was observed in the PVA/MTX group, which produced an inhibition zone of 18.02 ± 0.40 mm. This value represents a significant improvement over both pure PVA ($p < 0.0001$) and the PLA/ZnO composite ($p < 0.001$). Although methotrexate is not a conventional antibacterial agent, the PVA-MTX scaffold exhibited measurable inhibition zones against both *E. coli* and *S. aureus*, particularly for *S. aureus*. This effect may be attributed to non-specific metabolic interference and the rapid diffusion of MTX from the hydrophilic PVA matrix, rather than a classical antibacterial mechanism. The hydrophilic nature of the PVA matrix allows for the rapid dissolution and release of MTX into the surrounding medium, creating a high local concentration of the drug that effectively penetrates the Gram-negative cell wall.

Against *S. aureus*, pure PLA scaffolds displayed a mean inhibition zone of 13.00 ± 0.00 mm. This value is notably higher than that observed for *E. coli*. The absence of an outer lipopolysaccharide (LPS) membrane in Gram-positive bacteria makes their peptidoglycan cell wall more permeable to physical interactions and potential acidic byproducts of PLA degradation (lactic acid oligomers), which may create a locally acidic environment unfavorable for bacterial proliferation. The PLA/ZnO composite demonstrated strong antibacterial activity with a zone of 18.23 ± 0.17 mm. This represents a statistically significant improvement over pure PLA ($p < 0.0001$). ZnO nanoparticles are known to have a higher affinity for Gram-positive bacteria due to the electrostatic attraction between the positively charged zinc ions (Zn^{2+}) and the negatively charged teichoic acids on the *S. aureus* surface. The disruption of membrane integrity and the inhibition of essential enzymatic functions by zinc ions contributed to the strong inhibitory effect observed. Interestingly, pure PVA showed a relatively high baseline activity against *S. aureus* (17.00 ± 0.00 mm). While PVA is non-toxic, the rapid hydration and swelling of the nanofibers might act as a dehydration sink, locally altering the osmotic balance essential for *S. aureus* survival. Additionally, the dense nanofiber

network may physically entrap bacterial cells, limiting their colony formation in the immediate vicinity of the disk. The PVA/MTX scaffold achieved the highest overall inhibition zone in the study, measuring 23.36 ± 0.45 mm. This result classifies the material as having "Very Strong" antibacterial activity. The synergistic effect of the rapid release of MTX from the PVA matrix and the high susceptibility of *S. aureus* to metabolic inhibition resulted in a substantial clearance zone. The statistical analysis confirms that this group is significantly superior to all other tested materials ($p < 0.0001$), suggesting its high potential for use in wound dressings where *S. aureus* infections are prevalent [40–42].

While both agents proved effective, MTX demonstrated superior performance in terms of zone diameter. ZnO relies on contact-mediated killing and ROS generation, which has a limited effective radius in a solid agar medium. Methotrexate, being a small-molecule drug with high solubility (especially when released from PVA), diffuses more freely, establishing a wider concentration gradient that inhibits bacterial growth at greater distances from the scaffold.

The study demonstrated that the incorporation of ZnO and MTX into polymeric nanofibers resulted in enhanced antibacterial effects, as evidenced by the inhibition zone measurements. The PVA/MTX scaffold emerged as the most potent formulation, exhibiting very strong activity against both *E. coli* and *S. aureus*. The PLA/ZnO scaffold also showed strong efficacy, particularly against Gram-positive bacteria, offering a viable alternative for applications requiring slower degradation or hydrophobic properties. These findings suggest that the fabricated nanocomposites are promising candidates for biomedical applications, such as infection-resistant wound dressings, where broad-spectrum antibacterial protection is critical.

3.8 | Cytotoxicity and Biocompatibility Analysis

To determine the safety of the produced materials for application on surgical wounds, the cytotoxicity of the dressings was evaluated using L929 mouse fibroblast cells over 14 days. The cell viability results for the PVA, PVA-MTX, PLA-ZnO, and the bilayer composite (PVA-MTX+PLA-ZnO) are presented in Figure 9.

The results indicate excellent biocompatibility across all sample groups. As shown in the graph, cell viability remained above 90% for all tested materials throughout the incubation period (Days 1, 5, 7, and 14), significantly exceeding the ISO 10993–5 threshold of 70% required to classify a material as non-cytotoxic.

Notably, the bilayer composite (PVA-MTX+PLA-ZnO) maintained cell viability above 100% at all time points, demonstrating its cytocompatibility and lack of inhibitory effects on cell proliferation. For instance, by Day 14, the bilayer group reached a viability peak significantly higher than the standalone PVA or PLA samples. This suggests a synergistic effect where the hierarchical structure of the dressing, combining the mechanical support of the 3D-printed scaffold with the ECM-mimicking architecture of the nanofiber, creates an optimal microenvironment for fibroblast attachment and growth [43, 44].

Furthermore, the inclusion of the chemotherapeutic agent MTX in the PVA fibers did not induce significant toxicity in the healthy L929 cells, as observed by the comparable viability between the PVA and PVA/MTX groups. This is a critical finding, confirming that the dosage and release of MTX from the dressing are safe for healthy tissue surrounding the surgical site. Similarly, the addition of ZnO to the PLA scaffold (PLA/ZnO) appeared to enhance cell viability compared to pure PLA, likely due to the known role of Zinc ions in promoting cellular metabolism and wound healing processes [45, 46].

The biological safety and metabolic compatibility of the bilayer wound dressing components were comprehensively evaluated through the MTT [3-(4,5-dimethylthiazol-2-yl)-2,5-diphenyltetrazolium bromide] colorimetric assay. This assessment is fundamental for determining the suitability of the integrated system for clinical dermal applications. As illustrated in the quantitative evaluation of L929 fibroblast metabolic activity (Figure 9), all experimental groups including the drug-loaded PVA-MTX nanofibers and the metal-oxide-incorporated PLA-ZnO scaffold exhibited viability percentages well above the 70% threshold defined by ISO 10993–5. In the initial 24-h period, the metabolic activity of cells cultured on the PVA-MTX nanofibers was statistically equivalent to the negative control ($p > 0.05$), indicating that the localized presence of methotrexate did not induce an acute cytotoxic response or hinder early-stage cellular attachment.

The longitudinal assessment of the samples revealed a consistent and robust proliferation trend across the 72-h study duration. As evidenced by the cell viability and proliferation trends (Figure 9A), the metabolic activity increased significantly in all groups from the 24-h to the 72-h mark (###$p < 0.001$). This sustained growth confirms that the bilayer architecture, specifically the nanofibrous interface, provides a biomimetic topography that facilitates continuous cellular expansion. At the 72-h interval, the PLA-ZnO scaffold and the bilayer interface groups exhibited a moderate reduction in the rate of proliferation compared to the pure polymer controls, with statistical significance levels of $**p < 0.01$ and $*p < 0.05$, respectively, as detailed in the statistical significance analysis (Figure 9B). This variation is attributed to the controlled release of Zn^{2+} ions from the scaffold matrix; while these ions provide a critical antimicrobial environment, their concentration at 72 h influences the rapid doubling time of fibroblasts without compromising overall viability or inducing apoptosis.

The integration of the two distinct manufacturing modalities electrospinning and 3D printing did not result in any antagonistic biological effects, confirming the biocompatibility of the hybrid fabrication approach. The metabolic activity of the integrated bilayer dressing remained high throughout the experimental period, demonstrating that the mechanical resilience of the 3D-printed layer and the high surface area of the nanofibers work synergistically to maintain a pro-regenerative microenvironment. The presence of methotrexate within the nanofibers did not interfere with the long-term proliferation capacity of the fibroblasts, suggesting that the drug release kinetics are well-synchronized with the cellular growth cycle. Consequently, the comprehensive data presented in Figure 9 confirms that the proposed bilayer system meets the stringent biological requirements for advanced

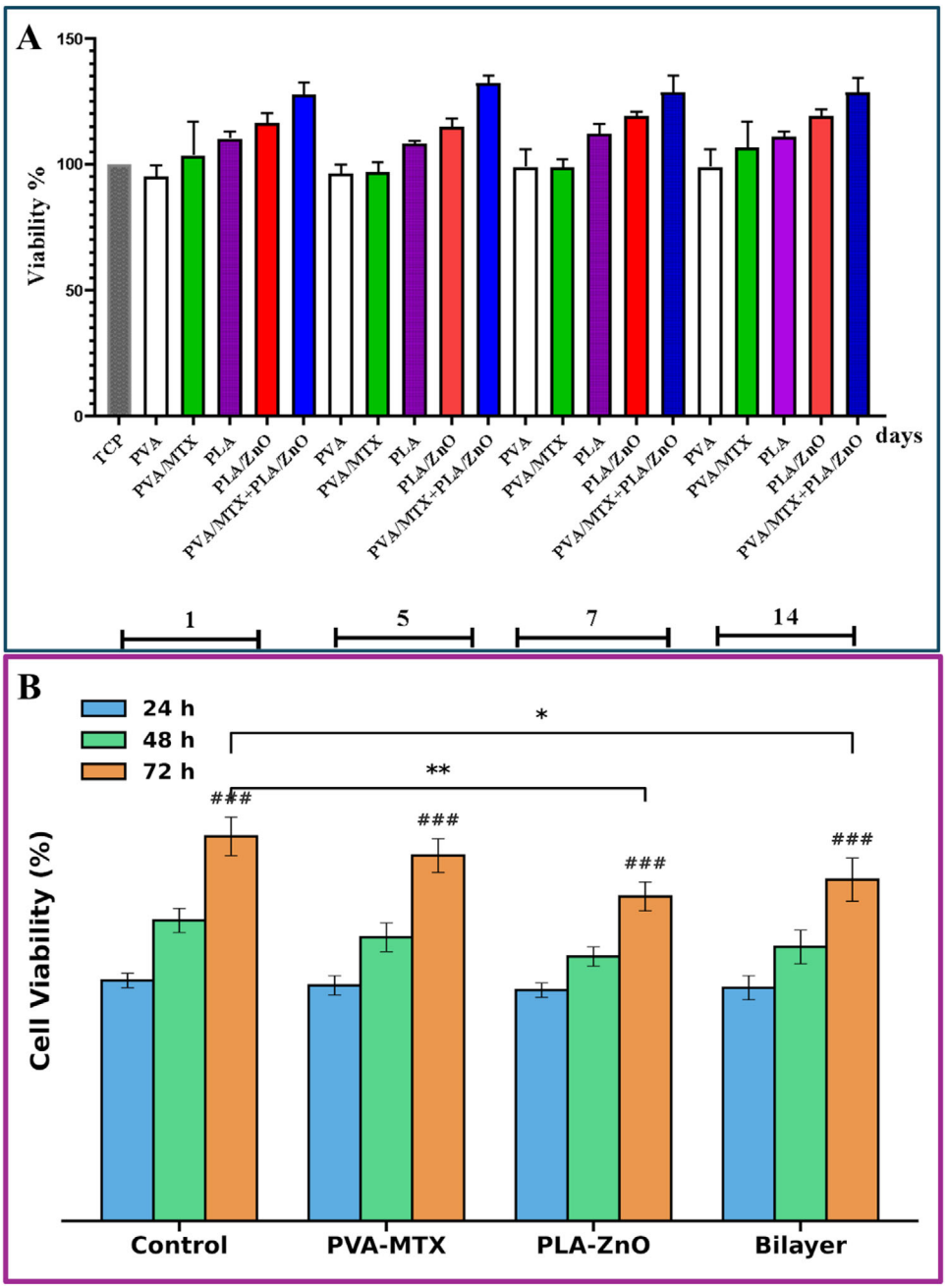

FIGURE 9 | Quantitative in vitro cytotoxicity and proliferation analysis of L929 fibroblast cells: A. Comparative cell viability percentages over 24, 48, and 72 h of incubation; B. Statistical significance analysis where significance levels are indicated as $*p < 0.05$ and $**p < 0.01$ compared to the negative control group, and ###p < 0.001 denoting significant time-dependent proliferation (72 h vs. 24 h).

wound management, providing a safe, therapeutically active, and supportive platform for dermal tissue regeneration.

4 | Conclusion

In this study, a multifunctional bilayer wound dressing was successfully developed by integrating electrospinning and 3D printing technologies, utilizing a green synthesis approach for the incorporation of therapeutic agents. The chemical and structural synergy of the system was confirmed through comprehensive characterization. FTIR and XRD analyses validated the successful molecular dispersion of methotrexate (MTX) within the PVA nanofibers and the crystalline integrity of the ZnO nanoparticles within the PLA scaffold. The absence of new crystalline phases in the XRD patterns and the preservation of characteristic vibrational modes in the FTIR spectra confirmed that the hybrid manufacturing process maintains the chemical identity of each component while fostering necessary molecular interactions.

Thermal and morphological evaluations provided further evidence of the system's stability. DSC analysis revealed that the drug loading and inorganic integration modulated the polymer crystallinity, with the bilayer system exhibiting enhanced

thermal stability compared to its individual components. SEM-EDS imaging demonstrated a bead-free nanofibrous architecture conformally adhered to a macro-porous 3D-printed framework, ensuring a high surface-area-to-volume ratio for biological interaction. The elemental mapping confirmed a uniform distribution of ZnO and MTX, which is critical for consistent therapeutic performance across the dressing interface.

The functional performance of the dressing was validated through mechanical and kinetic studies. Mechanical testing illustrated that the 3D-printed PLA-ZnO struts provided the requisite structural resilience, significantly reinforcing the delicate PVA-MTX matrix without compromising flexibility. This mechanical robustness was complemented by the drug release studies, where mathematical modeling confirmed a non-Fickian diffusion mechanism. This ensures a controlled and sustained release of MTX, providing a predictable therapeutic window for managing wound-site inflammation. Furthermore, the antibacterial assays demonstrated that the green-synthesized ZnO particles effectively inhibited pathogen proliferation, providing a secondary layer of protection against exogenous infections.

The biological safety of the integrated platform was confirmed through MTT cytotoxicity assays, where L929 fibroblast cells maintained high viability and consistent proliferation rates over 72 h. The adherence to ISO 10993–5 standards proves that the synergistic combination of MTX and ZnO, incorporated via eco-friendly modalities, does not induce adverse cellular responses. In conclusion, the developed bilayer dressing represents a technologically advanced and biocompatible management platform. By successfully bridging the gap between mechanical durability and biomimetic drug delivery through a green synthesis framework, this system offers a promising and sustainable strategy for the treatment of complex dermal wounds.

Acknowledgements

The authors would like to thank Fatih Sultan Mehmet Vakif University Aluminum Testing Training and Research Center (ALUTEAM) and the Foundation Center for the Protection, Implementation and Research of Cultural Heritage (KURAM) for their institutional support. The authors also gratefully acknowledge TÜBİTAK ULAKBİM for article processing charge (APC) support.

Conflicts of Interest

The authors declare no conflicts of interest.

Data Availability Statement

The data that support the findings of this study are available from the corresponding author upon reasonable request.

References

1. J. M. Taber, B. A. Dickerman, J.-P. Okhovat, et al., "Skin Cancer Interventions Across the Cancer Control Continuum: Review of Technology, Environment, and Theory," *Preventive Medicine* 111 (2018): 451–458, https://doi.org/10.1016/j.ypmed.2017.12.019.

2. A. H. Roky, M. M. Islam, A. M. F. Ahasan, et al., "Overview of Skin Cancer Types and Prevalence Rates Across Continents," *Cancer Pathogenesis and Therapy* 3, no. 2 (2025): 89–100, https://doi.org/10.1016/j.cpt.2024.08.002.

3. T. I. Pavel, C. Chircov, M. Rădulescu, and A. M. Grumezescu, "Regenerative Wound Dressings for Skin Cancer," *Cancers* 12, no. 10 (2020): 1–22, https://doi.org/10.3390/cancers12102954.

4. Z. Yu, H. Wu, X. Zhang, et al., "Antibacterial and Biodegradable Bandage With Exudate Absorption and Smart Monitoring for Chronic Wound Management," *Journal of Bioresources and Bioproducts* 10, no. 3 (2025): 373–385, https://doi.org/10.1016/j.jobab.2025.06.001.

5. D. Gao, W. D. Shipman, Y. Sun, J. Z. Glahn, L. Beraki, and H. C. Hsia, "Macroporous Scaffolds Based on Biomass Polymers and Their Applications in Wound Healing," *Journal of Bioresources and Bioproducts* 10, no. 1 (2025): 14–31, https://doi.org/10.1016/j.jobab.2024.12.001.

6. G. Kathiresan, K. Adaikalam, and H. S. Kim, "Advantages of Electrospinning Biomimetic Scaffolds for the Current Trend of Tissue Engineering Applications," *Journal of Applied Polymer Science* 142, no. 33 (2025): 57309, https://doi.org/10.1002/app.57309.

7. F. Ciftci, "Release Kinetics Modelling and in Vivo-vitro, Shelf-life Study of Resveratrol Added Composite Transdermal Scaffolds," *International Journal of Biological Macromolecules* 235 (2023): 123769, https://doi.org/10.1016/J.IJBIOMAC.2023.123769.

8. Z. Sadrearhami, M. Morshed, and J. Varshosaz, "Production and Evaluation of Polyblend of Agar and Polyacrylonitrile Nanofibers for in Vitro Release of Methotrexate in Cancer Therapy," *Fibers and Polymers* 16, no. 2 (2015): 254–262, https://doi.org/10.1007/s12221-015-0254-z.

9. S. Hashemi, S. A. Mortazavi, H. R. Moghimi, and B. Darbasizadeh, "Development and Evaluation of a Novel Methotrexate-loaded Electrospun Patch to Alleviate Psoriasis Plaques," *Drug Development and Industrial Pharmacy* 48, no. 8 (2022): 355–366, https://doi.org/10.1080/03639045.2022.2117373.

10. S. Yücer, B. Sarac, E. Karaduman, A. Erarslan, and F. Ciftci, "3D bioprinting Scaffold of Gelatine Reinforced-zinc Nanoparticles Synthesized by Green Synthesis: Comparative Evaluation of Mechanical and Thermal Properties," *Journal of Molecular Structure* 1357 (2026): 145214, https://doi.org/10.1016/j.molstruc.2025.145214.

11. O. Tavukcuoglu, N. E. Duygulu, A. Altinbay, and F. Ciftci, "Green Synthesis of Silver Nanoparticles From Thymus Vulgaris and Sambucus Nigra Extracts in Poly (vinyl alcohol) Nanofiber Matrix: In Vitro Evaluation," *Industrial Crops and Products* 222 (2024): 119825, https://doi.org/10.1016/J.INDCROP.2024.119825.

12. O. Tavukcuoglu, F. Ciftci, N. E. Duygulu, D. Misirli, M. Elmastas, and I. Isildak, "Green-Synthesized Silver Nanoparticles From Black Elderberry Extract as Potential TMPRSS2 Inhibitors: Implications for SARS-CoV-2 Antiviral Therapeutics," *Materials Today Communications* 48 (2025): 113609, https://doi.org/10.1016/j.mtcomm.2025.113609.

13. B. Oktay, F. Ciftci, A. Erarslan, and E. A. Özerol, "Dual-Layer Natamycin and Boric-Acid-Reinforced PVA/Chitosan by 3D Printing and Electrospinning Method: Characterization and in Vitro Evaluation," *Polymers* 17, no. 12 (2025): 1673, https://doi.org/10.3390/polym17121673.

14. M. N. Özder, A. Yelkenci, M. Kucak, A. Altinbay, C. B. Ustündag, and F. Ciftci, "Development and Characterization of a Polycaprolactone/Graphene Oxide Scaffold for Meniscus Cartilage Regeneration Using 3D Bioprinting," *Pharmaceutics* 17, no. 3 (2025): 346, https://doi.org/10.3390/pharmaceutics17030346.

15. E. F. D. Reis, F. S. Campos, A. P. Lage, et al., "Synthesis and Characterization of Poly (vinyl alcohol) Hydrogels and Hybrids for rMPB70 Protein Adsorption," *Materials Research* 9, no. 2 (2006): 185–191, https://doi.org/10.1590/s1516-14392006000200014.

16. R. Shah and S. Bhattacharya, "Preparation and Physical Characterization of Methotrexate Encapsulated Poly (n-methyl glycine) Microspheres for the Rheumatoid Arthritis Treatment Option," *Results in Chemistry* 5 (2023): 100875, https://doi.org/10.1016/j.rechem.2023.100875.

17. A. Enumo, I. P. Gross, R. H. Saatkamp, A. T. N. Pires, and A. L. Parize, "Evaluation of Mechanical, Thermal and Morphological

Properties of PLA Films Plasticized With Maleic Acid and Its Propyl Ester Derivatives," *Polymer Testing* 88 (2020): 106552, https://doi.org/10.1016/j.polymertesting.2020.106552.

18. B. Mulyati, F. Gapsari, S. Fiddaroini, and A. Sabarudin, "PLA/ZnO Nanocomposites With 0.05% w/v ZnO Enhanced Long-term Corrosion Inhibition of Low Carbon Steel," *South African Journal of Chemical Engineering* 54 (2025): 397–417, https://doi.org/10.1016/j.sajce.2025.09.003.

19. B. Liu, L. Yang, H. Yang, et al., "A Biomimetic Multifunctional Dressing Based on Stratum Corneum Microstructure: Integrating Antibacterial Barrier and Breathability for Enhanced Wound Healing," *Biomaterials* 326 (2026): 123639, https://doi.org/10.1016/j.biomaterials.2025.123639.

20. A. Vijayan, C. K. Nanditha, and G. S. Vinod Kumar, "ECM-mimicking Nanofibrous Scaffold Enriched With Dual Growth Factor Carrying Nanoparticles for Diabetic Wound Healing," *Nanoscale Advances* 3, no. 11 (2021): 3085–3092, https://doi.org/10.1039/d0na00926a.

21. L. C. Rodriguez-Pacheco, D. Lardizabal-Gutierrez, J. C. Pantoja-Espinoza, L. De La Torre-Saenz, I. A. Estrada-Moreno, and F. Paraguay-Delgado, "Novel 3D Printing filaments: PLA and Zinc Carbonate Basic Composites for Laser-assisted Thermal Decomposition," *Journal of Materials Research and Technology* 31 (2024): 2266–2278, https://doi.org/10.1016/j.jmrt.2024.06.237.

22. W. J. Chong, P. Wright, D. P. Simunec, et al., "A Comprehensive Study on the Biodegradability, Biocompatibility, and Antibacterial Properties of Additively Manufactured PLA-ZnO Nanocomposites," *Smart Materials in Manufacturing* 3 (2025): 100069, https://doi.org/10.1016/j.smmf.2024.100069.

23. I. R. D. Abreu, R. D. S. Nascimento Junior, A. G. D. S. Fortes, et al., "Thermal and mechanical properties of filaments for additive manufacturing," *Polímeros* 34, no. 3 (2024): 20240025, https://doi.org/10.1590/0104-1428.20240034.

24. Z. Chu, T. Zhao, L. Li, J. Fan, and Y. Qin, "Characterization of Antimicrobial Poly (lactic acid)/Nano-composite Films With Silver and Zinc Oxide Nanoparticles," *Materials* 10, no. 6 (2017): 659, https://doi.org/10.3390/ma10060659.

25. C. Rachtanapun, J. Sukunta, K. Jantanasakulwong, S. Thanakkasaranee, J. Tantala, and P. Rachtanapun, "Enhancing Antimicrobial Properties and Hydrophilicity of Environmentally Biodegradable Plastic Using Sparking-Deposited ZnO Nanoparticles," *Food Bioscience* 71 (2025): 107077, https://doi.org/10.1016/j.fbio.2025.107077.

26. A. Rezaei, E. Katoueizadeh, and S. M. Zebarjad, "Investigating of the Influence of Zinc Oxide Nanoparticles Morphology on the Properties of Electrospun Polyvinyl Alcohol/Chitosan (PVA/CS) Nanofibers," *Journal of Drug Delivery Science and Technology* 86 (2023): 104712, https://doi.org/10.1016/j.jddst.2023.104712.

27. E. R. Kenawy, E. A. Kamoun, A. Shehata, S. H. El-Moslamy, and A. A. H. Abdel-Rahman, "Biosynthesized ZnO NPs Loaded-electrospun PVA/Sodium Alginate/Glycine Nanofibers: Synthesis, Spinning Optimization and Antimicrobial Activity Evaluation," *Scientific Reports* 15, no. 1 (2025): 1882, https://doi.org/10.1038/s41598-024-81939-1.

28. P. Gopinath, P. Suresh, and V. Jeevanantham, "Mechanical, Structural and Optical Properties of Pristine and PVA Capped Zinc Oxide Nanocomposites," *Journal of Ovonic Research* 19, no. 1 (2023): 23–30, https://doi.org/10.15251/JOR.2023.191.23.

29. A. M. Hezma, A. Rajeh, and M. A. Mannaa, "An Insight Into the Effect of Zinc Oxide Nanoparticles on the Structural, Thermal, Mechanical Properties and Antimicrobial Activity of Cs/PVA Composite," *Colloids and Surfaces A: Physicochemical and Engineering Aspects* 581 (2019): 123821, https://doi.org/10.1016/j.colsurfa.2019.123821.

30. S. A. Shah, H. Ali, M. I. Inayat, E. E. Mahmoud, H. A. Garalleh, and B. Ahmad, "Effect of Carbon Nanotubes and Zinc Oxide on Electrical and Mechanical Properties of Polyvinyl Alcohol Matrix Composite by Electrospinning Method," *Scientific Reports* 14, no. 1 (2024): 28107, https://doi.org/10.1038/s41598-024-79477-x.

31. Y. D. Nokoorani, A. Shamloo, M. Bahadoran, and H. Moravvej, "Fabrication and Characterization of Scaffolds Containing Different Amounts of Allantoin for Skin Tissue Engineering," *Scientific Reports* 11 (2021): 1–20, https://doi.org/10.1038/s41598-021-95763-4.

32. D. Enrique, L. Angulo, and P. José, "International Journal of Biological Macromolecules Characterization of Gelatin /Chitosan Scaffold Blended With Aloe Vera and Snail Mucus for Biomedical Purpose," *International Journal of Biological Macromolecules* 92 (2016): 645–653, https://doi.org/10.1016/j.ijbiomac.2016.07.029.

33. N. Abuhamed, S. Arslan, K. E. Öksüz, and E. Dinçer, "From Biopolymer Matrix to Medicine: The Drug Delivery Dynamics of Amoxicillin-loaded PVA/SA/ZnONPs Hydrogels," *International Journal of Polymeric Materials and Polymeric Biomaterials* 74, no. 6 (2025): 484–496, https://doi.org/10.1080/00914037.2024.2351851.

34. R. Niranjan, M. Kaushik, J. Prakash, et al., "Chitosan Based Wound Dressing Patch Loaded With Curcumin Tagged ZnO Nanoparticles for Potential Wound Healing Application," *Inorganic Chemistry Communications* 154 (2023): 110885, https://doi.org/10.1016/j.inoche.2023.110885.

35. M. Sadeghi-Aghbash, M. Rahimnejad, H. Adeli, and F. Feizi, "Catecholamines Polymerization Crosslinking for Alginate-based Burn Wound Dressings Developed With Ciprofloxacin and Zinc Oxide Interactions," *International Journal of Biological Macromolecules* 260 (2024): 129400, https://doi.org/10.1016/j.ijbiomac.2024.129400.

36. S. Baghaie, M. T. Khorasani, A. Zarrabi, and J. Moshtaghian, "Wound Healing Properties of PVA/Starch/Chitosan Hydrogel Membranes With Nano Zinc Oxide as Antibacterial Wound Dressing Material," *Journal of Biomaterials Science, Polymer Edition* 28, no. 18 (2017): 2220–2241, https://doi.org/10.1080/09205063.2017.1390383.

37. Y. Gutha, J. L. Pathak, W. Zhang, Y. Zhang, and X. Jiao, "Antibacterial and Wound Healing Properties of Chitosan/Poly(vinyl alcohol)/Zinc Oxide Beads (CS/PVA/ZnO)," *International Journal of Biological Macromolecules* 103 (2017): 234–241, https://doi.org/10.1016/j.ijbiomac.2017.05.020.

38. H. Elgharbawy, A. Hassona, M. A. Eid, and R. Morsy, "Synthesis and Biophysical Characterization of Porous bi-phase Calcium Phosphate/Gelatin-PVA Scaffold: Enhanced Antibacterial, Osteoconductivity and Anticancer Activity via Silver Nanoparticles and Methotrexate Incorporation," *Journal of Molecular Structure* 1311 (2024): 138329, https://doi.org/10.1016/j.molstruc.2024.138329.

39. F. B. Zeynabad, R. Salehi, and M. Mahkam, "Design of pH-responsive Antimicrobial Nanocomposite as Dual Drug Delivery System for Tumor Therapy," *Applied Clay Science* 141 (2017): 23–35, https://doi.org/10.1016/j.clay.2017.02.015.

40. K. Kikuchi, R. Miyauchi, T. Yamaguchi, et al., "An Experimental Study on the Addition of Bacteria to Residual Anticancer Drugs: Evaluation of the Effect on Bacterial Growth," *Japanese Journal of Infectious Diseases* 77, no. 2 (2024): 61–67, https://doi.org/10.7883/yoken.JJID.2023.270.

41. N. G. M. Attallah, F. A. Mokhtar, E. Elekhnawy, et al., "Mechanistic Insights on the in Vitro Antibacterial Activity and in Vivo Hepatoprotective Effects of Salvinia Auriculata Aubl Against Methotrexate-Induced Liver Injury," *Pharmaceuticals* 15, no. 5 (2022): 549, https://doi.org/10.3390/ph15050549.

42. A. M. Mohammed, S. K. Osman, K. I. Saleh, and A. M. Samy, "In Vitro Release of 5-Fluorouracil and Methotrexate From Different Thermosensitive Chitosan Hydrogel Systems," *AAPS Pharmscitech* 21, no. 4 (2020): 131, https://doi.org/10.1208/s12249-020-01672-6.

43. J. I. Kim, J. Y. Kim, G. Bhattarai, H. S. So, S. H. Kook, and J. C. Lee, "Erratum: Periodontal Ligament-Mimetic Fibrous Scaffolds Regulate YAP-Associated Fibroblast Behaviors and Promote Regeneration of Periodontal Defect in Relation to the Scaffold Topography," *ACS Applied Materials and Interfaces* 15, no. 15 (2023): 19783, https://doi.org/10.1021/acsami.3c03393.

44. J. I. Kim, J. Y. Kim, G. Bhattarai, H. S. So, S. H. Kook, and J. C. Lee, "Periodontal Ligament-Mimetic Fibrous Scaffolds Regulate YAP-Associated Fibroblast Behaviors and Promote Regeneration of Periodontal Defect in Relation to the Scaffold Topography," *ACS Applied Materials & Interfaces* 15, no. 1 (2023): 599–616, https://doi.org/10.1021/acsami.2c18893.

45. N. H. Gomaa, N. K. A. El-Aziz, E. Sayed, Y. El-Naenaeey, W. S. Abdelaziz, and A. H. Sewid, "Antimicrobial Potential of Myricetin-coated Zinc Oxide Nanocomposite Against Drug-resistant Clostridium Perfringens," *BMC Microbiology* 23, no. 1 (2023): 79, https://doi.org/10.1186/s12866-023-02800-5.

46. O. A. Tosyali, F. Sahin, Y. Cetin, and O. Karal-Yilmaz, "Fabrication and Characterization of Amphotericin B Loaded Poly(Vinyl Alcohol)/Chitosan- ZnO Biocomposite Films for Antimicrobial Wound Dressings," *Journal of Applied Polymer Science* 142, no. 8 (2025): 56517, https://doi.org/10.1002/app.56517.